

Provided for non-commercial research and education use.  
Not for reproduction, distribution or commercial use.



This article appeared in a journal published by Elsevier. The attached copy is furnished to the author for internal non-commercial research and education use, including for instruction at the authors institution and sharing with colleagues.

Other uses, including reproduction and distribution, or selling or licensing copies, or posting to personal, institutional or third party websites are prohibited.

In most cases authors are permitted to post their version of the article (e.g. in Word or Tex form) to their personal website or institutional repository. Authors requiring further information regarding Elsevier's archiving and manuscript policies are encouraged to visit:

<http://www.elsevier.com/copyright>



Contents lists available at ScienceDirect

## Earth and Planetary Science Letters

journal homepage: [www.elsevier.com/locate/epsl](http://www.elsevier.com/locate/epsl)

## Global variations of temperature and water content in the mantle transition zone from higher mode surface waves

U. Meier<sup>a,\*</sup>, J. Trampert<sup>a</sup>, A. Curtis<sup>b,c</sup><sup>a</sup> Utrecht University, Department of Earth Sciences, Seismology, Budapestlaan 4, 3584 CD Utrecht, The Netherlands<sup>b</sup> University of Edinburgh, School of GeoSciences, Grant Institute, The King's Buildings, West Mains Road, Edinburgh EH9 3JW, UK<sup>c</sup> Edinburgh Collaborative of Subsurface Science and Engineering, Edinburgh, UK

## ARTICLE INFO

## Article history:

Received 22 September 2008

Received in revised form 27 February 2009

Accepted 2 March 2009

Available online 28 March 2009

Editor: R.D. van der Hilst

## Keywords:

transition zone  
nonlinear inversion  
surface waves  
tomography

## ABSTRACT

We performed a fully nonlinear joint inversion of surface wave overtone phase velocities for velocity structure down to a depth of 1500 km and topography of transition zone discontinuities using neural networks. The resulting models are compared with existing mantle models from linearized inversions techniques and the agreement between vertically averaged S-wave velocity models and various 660-km topography models is very good, whereas the agreement between all the 400-km topography models is very poor. The latter might be due to a broader than previously reported 400-km discontinuity where the minerals co-exist with water induced melt. From our models of transition zone thickness and S-wave velocity we estimated lateral variations of temperature and water content in Earth's mantle transition zone, linearly relating variations in S-wave velocity and transition zone thickness to variations in temperature and water content. Within the transition zone we observe relatively cold subduction zones as well as relatively warm regions beneath continents and hot spots. We find that the transition zone is wettest away from subduction zones.

©2009 Elsevier B.V. All rights reserved.

## 1. Introduction

The nature of Earth's transition zone is central to the understanding of mantle dynamics. Its vertical extent is bounded by two seismic discontinuities, herein referred to as the 400- and 660-km discontinuities, usually attributed to phase transitions from olivine to wadsleyite and from ringwoodite to perovskite and magnesiowüstite, respectively (see Helffrich, 2000; Shearer, 2000, for reviews). These two phase transitions have different pressure–temperature stability fields for hydrous and anhydrous conditions (Litasov et al., 2006; Smyth and Jacobsen, 2006). Experimental studies have shown that the presence of water shifts the 660-km phase transformation boundary towards higher pressure but does not affect its broadness (Litasov et al., 2006). Thermodynamical modeling revealed that the stability field of the phase transition associated with the 400-km discontinuity broadens with increasing water content from  $\approx 7$  km (dry) to a maximum of 24 km (saturation level of olivine), and that a further increase in water content causes partial melting with a corresponding thinning of the transition interval (Hirschmann et al., 2006). These calculations are in agreement with experimental studies that ob-

served a 400-km discontinuity as broad as 20 km under hydrous conditions (Litasov et al., 2006; Frost and Dolejš, 2007).

The so-called transition zone between the 400-km and 660-km discontinuities could be a significant water reservoir (Bercovici and Karato, 2003). If the water concentration in the transition zone exceeds the storage capacity of upper mantle olivine, the water filter model predicts a 2–20 km thick melt layer lying on top of the 400-km discontinuity which plays a fundamental role in geochemical cycling and mantle dynamics (Bercovici and Karato, 2003). Regional seismic studies have reported a low-velocity layer on top of the 400-km discontinuity attributed to such a partially molten layer (Song et al., 2004; Jasbinsek and Dueker, 2007) and isolated regions of high water content in the transition zone (van der Meijde et al., 2003; Suetsugu et al., 2006). We present a new global model of temperature and water content variations in the mantle transition zone based on the consistent modeling of new seismic data.

Upper mantle discontinuities are usually probed by analyzing seismic phases that reflect and convert at these discontinuities. The most important ones are SS or PP precursors from underside reflections (e.g. Shearer and Masters, 1992; Petersen et al., 1993; Gossler and Kind, 1996; Gu et al., 1998; Flanagan and Shearer, 1998a; Flanagan and Shearer, 1999; Deuss and Woodhouse, 2001, 2002; Gu and Dziewonski, 2002; Chambers et al., 2005; Schmerr and Garnero, 2006; Schmerr and Garnero, 2007), near-receiver P-to-S converted phases (e.g. Flanagan and Shearer, 1998b; Chevrot et al., 1999; Lebedev et al., 2002; Lebedev et al., 2003; Lawrence and Shearer, 2006; Tauzin

\* Corresponding author. Institut de Physique du Globe de Paris, Equipe de Sismologie, 4 Place, Jussieu Case 89, 75252 Paris cedex 05, France. Tel.: +33 144272469; fax: +33 144273894.

E-mail addresses: [meierue@geo.uu.nl](mailto:meierue@geo.uu.nl) (U. Meier), [jeannot@geo.uu.nl](mailto:jeannot@geo.uu.nl) (J. Trampert), [andrew.curtis@ed.ac.uk](mailto:andrew.curtis@ed.ac.uk) (A. Curtis).

et al., 2008) and near source S-to-P converted phases (e.g. Vidale and Benz, 1992; Collier and Helffrich, 1997). Near-source conversions only illuminate the discontinuity in the vicinity of earthquakes and near-receiver conversions only below areas of seismic stations. Converted phases are therefore only useful for local studies but with a relatively high lateral resolution of 100 km or less (Lebedev et al., 2003). Underside reflections of SS and PP phases on the other hand interact with the discontinuities at the midpoint between source and receiver, resulting in a reasonable global data coverage. The lateral resolution is assumed to be of several thousand km, but is difficult to quantify because stacking is involved. Obtaining absolute depth estimates from underside reflections or converted phases requires an accurate velocity model, therefore uncertainties in velocity models map directly into uncertainties in topography. This is unsatisfactory, especially because most velocity models are obtained assuming fixed discontinuities. It is therefore desirable to perform a joint inversion for mantle velocity structure and topography but this has only been attempted using a linearized approach (Gu et al., 2003). Another approach has recently been proposed by Ritsema et al. (2008), who used mineral physics based calculations of upper mantle shear velocity to compute differential traveltimes of shear wave reflections off the 410-km and 660-km discontinuities and compared those directly to values measured from broadband waveforms.

We took a different approach and performed a nonlinear joint inversion for velocity structure and transition zone discontinuities using surface wave overtone measurements of Rayleigh waves up to the sixth higher mode and of Love waves up to the fifth higher mode (Visser et al., 2008a), data never before employed in studies of mantle discontinuities. As opposed to fundamental mode surface waves that are mostly sensitive to the upper 200 km, sensitivities of higher mode surface waves extend well into the lower mantle and make them especially suitable for mantle tomography (e.g. Ritsema et al., 2004; Visser et al., 2008b). We inverted these measurements using a neural network approach to obtain full Bayesian posterior probability density functions (pdfs) for the depth of the 400- and 660-km discontinuities, the transition zone thickness, as well as S-wave velocity, averaged over three different depth ranges in the upper mantle. A Mixture Density Network (MDN) (Bishop, 1995) was used to capture the full nonlinearity of the inverse problem, and readily allows us to calculate any desired statistic for any chosen model parameter (Meier et al., 2007a,b). From our models of vertically averaged S-wave velocity and transition zone thickness we infer lateral variations in temperature and water content, assuming a linear relationship between the seismic parameters (S-wave velocity, transition zone thickness) and the target parameters (temperature, water content) (Shito et al., 2006; Suetsugu et al., 2006). The coefficients of this linear relation, the partial derivatives of the seismic parameters with respect to the target parameters are adopted from experimental studies (Stixrude and Lithgow-Bertelloni, 2005; Litasov et al., 2006; Smyth and Jacobsen, 2006).

## 2. Data

The data used in this study consists of fundamental and higher mode isotropic phase velocity maps of Rayleigh and Love waves (Visser et al., 2008a). In the construction of these maps it is assumed that the phase perturbations with respect to a reference phase, acquired between source and receiver, are approximately given by the summation of local phase velocity perturbations along the great circle path (Woodhouse, 1974). As has been shown by Trampert and Spetzler (2006) the current data coverage is such that a better forward theory is not essential. From these phase velocity maps we extract local dispersion curves at specific periods (Table S1) up to the sixth higher mode for Rayleigh waves and up to the fifth higher mode for Love waves. The phase velocity maps are expanded in spherical harmonics and we evaluate them up to spherical harmonic degree 8 at 492 geographical locations on the Earth's surface distributed accord-

ing to a 6-fold triangular tessellation, equal area representation (Wang and Dahlen, 1995).

The uncertainties on the dispersion curves are assumed to be Gaussian:

$$\rho(\mathbf{d}) = \frac{1}{(2\pi)^{c/2} |\mathbf{C}_D|^{1/2}} \exp \left\{ -\frac{1}{2} (\mathbf{d}_{\text{obs}} - \mathbf{d})^T \mathbf{C}_D^{-1} (\mathbf{d}_{\text{obs}} - \mathbf{d}) \right\}, \quad (1)$$

where  $c=149$  is the dimension of  $\mathbf{d}$ , and corresponds to all phase velocity measurements at different periods (Table S1) for all the Rayleigh and Love wave modes.  $\mathbf{d}$  is the mean value of the distribution and the covariance matrix  $\mathbf{C}_D$  is assumed to be diagonal with the standard deviations for all the modes provided by Visser et al. (2008a). Note that these standard deviations used as a prior here are in fact posterior uncertainties of the phase velocity maps. Adopting a Bayesian approach we make sure that all the uncertainties in this two-step inversion are correctly transmitted to the resulting posterior pdfs.

## 3. Model parameterization

We invert local dispersion curves constructed from the phase velocity maps at the chosen 492 locations for local 1-D Earth structure and adopt a layered parameterization with depth. Given the period range and the sensitivities of the various modes we decided to fix our model to PREM (Dziewonski and Anderson, 1981) below a depth of 1500 km. From 1500 km depth up to the Moho we allow for radial anisotropy over the whole depth range (i.e. density ( $\rho$ ), vertically ( $V_{pv}$ ) and horizontally ( $V_{ph}$ ) polarized P-wave velocities, vertically ( $V_{sv}$ ) and horizontally polarized S-wave velocities ( $V_{sh}$ ) as well as the anisotropic parameter ( $\eta$ ) are allowed to vary (Dziewonski and Anderson, 1981). Our models consist of 24 layers from 1500 km depth up to the 660-km discontinuity, 8 layers within the transition zone between the 660- and 400-km discontinuities, 9 layers between the 400-km and 220-km discontinuity and 8 layers from 220 km depth up to the Moho. There are three crustal layers and a sedimentary layer with variable thickness on top of the crust. While we do not actually invert the data for the values of all of these parameters, all are allowed to vary in our inversions as explained below.

We use the same prior ranges for crustal  $\rho$ ,  $V_p$ ,  $V_s$  and Moho depth as in Meier et al. (2007b). The 220-km discontinuity is allowed to vary  $\pm 20$  km from its reference value and the 400- and 660-km discontinuities are allowed to vary  $\pm 30$  km from their respective reference values. In order to avoid highly oscillating and physically implausible models, we introduce correlations between adjacent layers. We decided to do that in the following way: at a discontinuity  $\rho$ ,  $V_{pv}$ ,  $V_{ph}$ ,  $V_{sv}$ ,  $V_{sh}$  and  $\eta$  are drawn independently from a uniform distribution. Adopting the same gradient as in PREM we compute the parameters of the next layer with increasing depth. We then add another perturbation on these values, effectively changing the PREM gradient within each layer. This procedure guarantees that in between the major discontinuities the resulting depth profiles have a gradient similar to that of PREM. At the Moho all the parameters are allowed to vary  $\pm 10\%$  of their corresponding PREM values, while the perturbation in each successive layer is  $\pm 2\%$  of the previous value. Between 220 km depth and the 400-km discontinuity and within the transition zone, the same procedure is repeated but at the discontinuity the values are allowed to vary  $\pm 5\%$  of PREM and the additional perturbations are  $\pm 1\%$ . Below the 660-km discontinuity we allow the parameters to vary  $\pm 2.5\%$  and  $\pm 0.5\%$  respectively. In this way we take into account that with increasing depth the lateral variations with respect to PREM generally decrease.

## 4. Forming the solution

We randomly generated 200 000 Earth models from the prior model pdf and for each we compute exact local synthetic dispersion curves using normal mode theory. For the normal mode approach, we used an algorithm developed by Woodhouse (1988) which allows the

computation of phase velocities of Rayleigh and Love waves in a 1-D model. We then design a MDN that takes the 149 phase velocities at various periods for all the modes of Rayleigh and Love waves as its input, and which models the Bayesian posterior pdf of the parameter of interest as a mixture of Gaussians. For a detailed description of the MDN the reader is referred to Meier et al. (2007a,b), who inverted fundamental mode surface waves for crustal structure using a MDN. In order to take the measurement errors into account we add Gaussian noise, using Eq. (1), to the exact dispersion curves and train the network on noisy dispersion curves. As demonstrated in Meier et al. (2007b), by the addition of noise the network mapping is implicitly constrained to be insensitive to small variations on the dispersion curves. Once a network is trained we can invert any set of dispersion curves within a fraction of a second by simply forward-propagating the set of dispersion curves through the trained network. For a detailed discussion about the network training the reader is referred to Meier et al. (2007b).

In this study we model marginal pdfs of the 400-, the 660-km topography and the transition zone thickness as well as isotropic S-wave Voigt averages  $V_s^2 = (2V_{sv}^2 + V_{sh}^2) / 3$  (Panning and Romanowicz, 2006). Our models are clearly over-parameterized with respect to the radial resolving power of the data. We therefore invert for isotropic S-wave speed, averaged over three different depth ranges; 1) averaged over the depth range between the Moho and the 220-km discontinuity referred to as the LID hereafter ( $V_s^{LID}$ ), 2) averaged over the depth range between the 220- and 400-km discontinuity referred to as the upper mantle hereafter ( $V_s^{UM}$ ) and 3) averaged over the depth range between the 400- and 660-km discontinuity referred to as the transition zone hereafter ( $V_s^{TZ}$ ).

Furthermore we estimate 2-D joint pdfs in order to analyze the trade-offs in the inversion. Consider the following decomposition of the joint pdf of 660-km topography and  $V_s^{TZ}$ ,

$$p(H_{.660}, V_s^{TZ} | \mathbf{d}) = p(H_{.660} | V_s^{TZ} | \mathbf{d}) p(V_s^{TZ} | \mathbf{d}). \quad (2)$$

where the vertical lines denote that these are conditional pdfs given fixed values of data  $\mathbf{d}$ . Using a first MDN that emulates  $p(V_s^{TZ} | \mathbf{d})$  and a second

MDN that takes  $V_s^{TZ}$  as an additional input and emulates  $p(H_{.660} | V_s^{TZ}, \mathbf{d})$  we have an approximation to the joint pdf  $p(H_{.660}, V_s^{TZ} | \mathbf{d})$ . Devilee et al. (1999) similarly used two histogram networks to approximate the joint pdf of crustal velocity and Moho depth.

## 5. Resolution analysis

In order to assess the reliability of the inversion algorithm, it is a common practice to invert synthetic data and compare the obtained results with the known underlying models. We do this by generating 10 000 additional models from the prior model pdf, which were not included in the training set, and compute the corresponding synthetic dispersion curves. We then invert the synthetic dispersion curves using trained MDNs and compare the network predictions with the known underlying models. Even though we invert exact local dispersion curves the MDNs were trained on noisy input curves in order to take the measurement uncertainties into account (Meier et al., 2007b). It is important to note that in generating the synthetic models, all model parameters were allowed to vary according to their prior pdfs.

### 5.1. 1-D marginals

In a first test we train three different networks on  $V_s^{LID}$ ,  $V_s^{UM}$  and  $V_s^{TZ}$ . Fig. 1 summarizes the resolution analysis in the LID (top), in the upper mantle (middle) and within the transition zone (bottom). The left hand column shows the posterior pdf (blue) obtained from the inversion of one particular set of dispersion curves from the test set together with the prior pdf for this parameter (red) and the known value of the underlying model (dashed). In the right column the mean from all 10 000 posterior pdfs is plotted against the known value of the underlying models. It is clearly visible that all three parameters are well resolved with respect to the prior pdf and that the mean network predictions correlate well with the known values. Not surprisingly with increasing depth the S-wave velocity is less well resolved as indicated by the decreasing correlation and the broadening of the scatter plots. The high correlations indicate

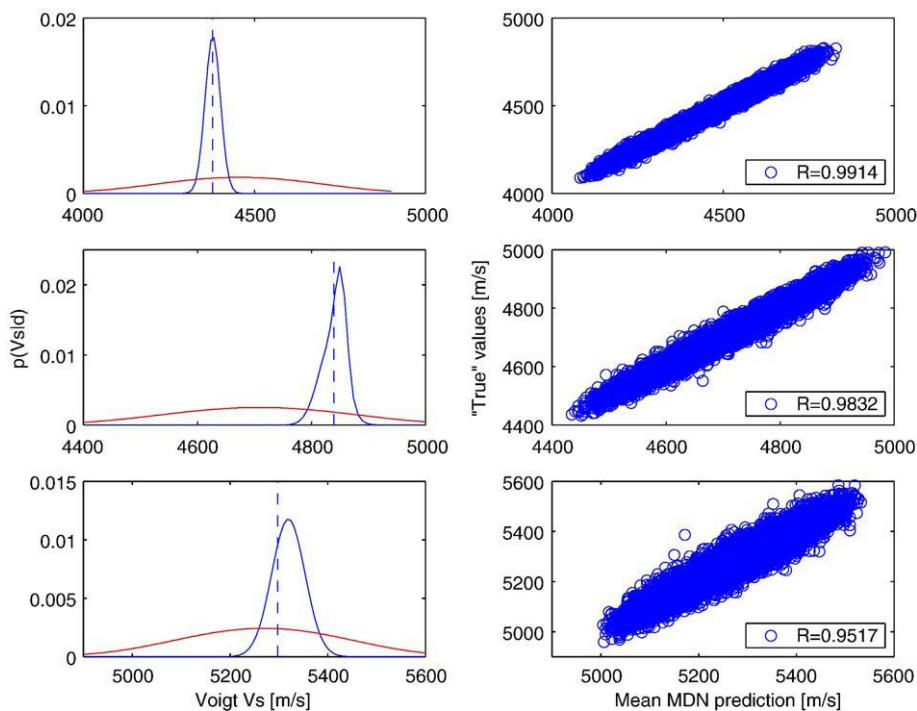


**Fig. 1.** Resolution analysis of S-wave Voigt averages in the LID (top), in the upper mantle (middle) and within the transition zone (bottom). (Left column) The posterior pdf (blue) obtained from the inversion of one particular set of dispersion curves from the test set is shown together with the prior pdf for this parameter (red) and the known value of the underlying model (dashed); (right column) the mean from all 10 000 posterior pdfs is plotted against the known value of the underlying models, together with the corresponding correlation coefficient R.

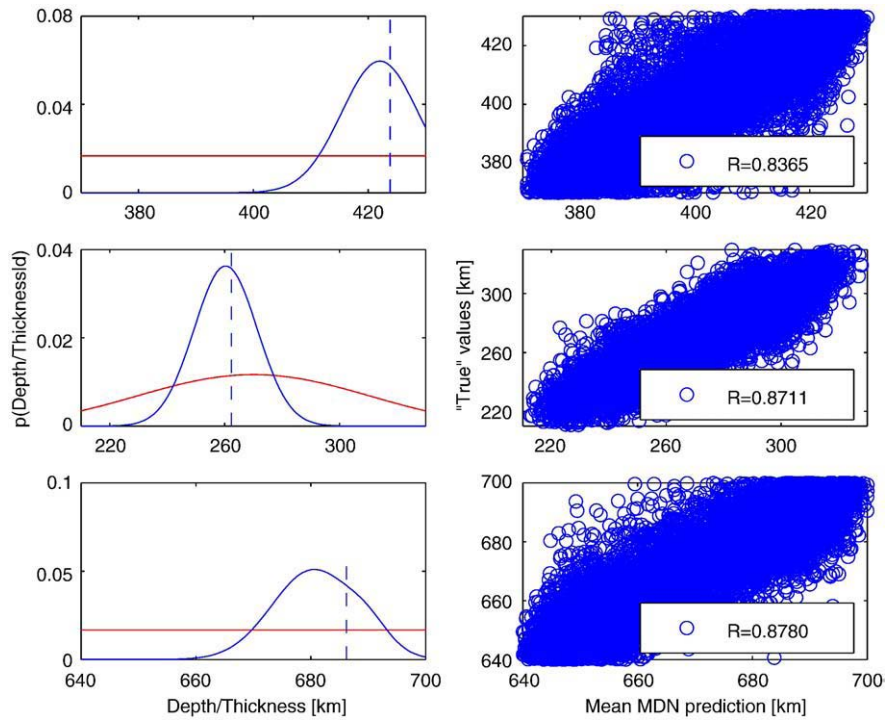


**Fig. 2.** Resolution analysis of the depth of the 400-km discontinuity (top), transition zone thickness (middle), and 660-km discontinuity depth (bottom). (Left column) The posterior pdf (blue) obtained from the inversion of one particular set of dispersion curves from the test set is shown together with the prior pdf for this parameter (red) and the known value of the underlying model (dashed); (right column) the mean from all 10 000 posterior pdfs is plotted against the known value of the underlying models together with the corresponding correlation coefficient  $R$ .

that for the given prior assumptions, noisy synthetic dispersion curves can be successfully inverted for  $V_s^{LD}$ ,  $V_s^{JM}$  and  $V_s^{TZ}$ . The inverted synthetic dispersion curves contain variations due to uncertainties in all of the model parameters, and the trade-offs between model parameters over

the a priori accessible model space together with the assumed measurement errors cause the posterior uncertainties.

We train three additional networks on the 400- and 660-km discontinuity as well as the transition zone thickness and perform the

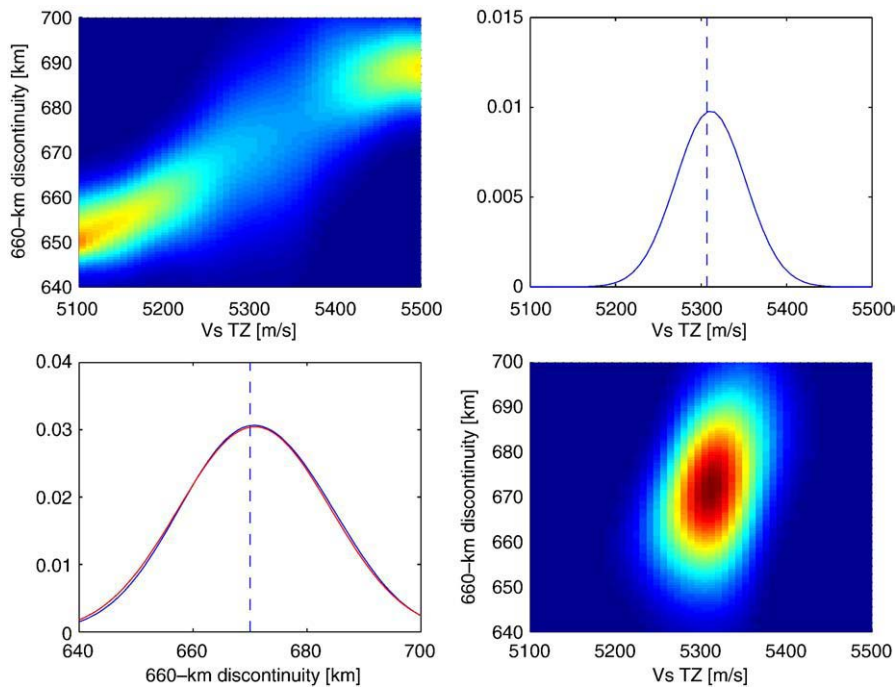


**Fig. 3.** (Top, left) Conditional pdfs of the 660-km topography conditioned on  $V_s^{TZ}$  as approximated by a MDN. (Top, right) Marginal pdf of  $V_s^{TZ}$  as approximated by a MDN together with the known velocity of the underlying model (dashed). (Bottom, left) Marginal pdf of the 660-km topography approximated by a MDN (blue) together with the marginal pdf obtained from the joint pdf (red) and the known depth of the underlying model (dashed). (Bottom, right) Joint pdf of the 660-km topography and  $V_s^{TZ}$  obtained according to the decomposition in Eq. (2). All the pdfs shown are conditional on  $\mathbf{d} = \mathbf{d}_{prem}$  and normalized such that they integrate to unity.

same analysis as above. Fig. 2 summarizes the resolution analysis where the depth of the 400-km discontinuity is shown at the top, the transition zone thickness in the middle, and depth of the 660-km discontinuity at the bottom. In the left column the posterior pdfs (blue) are shown together with the prior pdfs (red) and the known value of the underlying model (dashed), whereas in the right column the mean from all 10 000 posterior pdfs is plotted against the known value of the underlying models. Compared to the S-wave Voigt averages it is obvious that the 400- and 660-km topographies are not that well constrained with respect to the prior pdfs, but on average the mean MDN predictions still correlate well with the known values of the underlying models. From the broadness of the scatter plots it seems that the transition zone thickness is the best resolved parameter, the 660-km discontinuity depth is slightly less well resolved and the 400-km discontinuity depth is the least resolved parameter. The broadness of the posterior pdfs (left, column) is caused by trade-offs between the various model parameters and the measurement uncertainties.

A good correlation between network predictions and the known values of the underlying model is a first requirement if we hope to invert observed data successfully. A lack of correlation indicates that the parameter of interest is not resolvable given the prior assumptions. Since the prior over the data space (i.e. the measurement uncertainties) is generally fixed for a given problem, the prior over the model space has to be adjusted in order to constrain the inversion better. Furthermore such an analysis serves as a debugging exercise: successfully inverting synthetic data indicates that the algorithm works.

### 5.2. 2-D joint pdfs

So far we only modeled marginal posterior pdfs of the individual parameter of interest and attributed the posterior uncertainties partly due to trade-offs between model parameters and partly due to the measurement uncertainties. In order to separate uncertainties from trade-offs in the inversion it is most illustrative to plot 2-D pdfs. Here we analyze trade-offs between velocity structure within the transition zone ( $V_s^{TZ}$ ) and the depth of the 660-km discontinuity by modeling the conditional posterior pdf  $p(H_{660}|V_s^{TZ}, \mathbf{d})$ , the marginal posterior pdf  $p(V_s^{TZ}|\mathbf{d})$ ,  $p(H_{660}|\mathbf{d})$ , and the corresponding 2-D joint posterior pdf  $p(H_{660}, V_s^{TZ}|\mathbf{d})$ . All these pdfs are conditional on a given set of dispersion curves. In order to be comparable to other studies we decided to show all the pdfs from the inversion of a set of dispersion curves computed from PREM ( $\mathbf{d} = \mathbf{d}_{\text{prem}}$ ). Note however that inverting a different set of dispersion curves might result in quite different pdfs.

In Fig. 3 all the pdfs are normalized such that they integrate to unity (i.e. each vertical slice of the conditional pdf (top, left) integrates to unity, whereas the joint pdf (bottom, right) is normalized such that the double integral integrates to unity). The conditional pdf  $p(H_{660}|V_s^{TZ}, \mathbf{d}_{\text{prem}})$  (top, left) shows that inverting  $\mathbf{d}_{\text{prem}}$  and assuming relatively (with respect to PREM) high/low  $V_s^{TZ}$ , the data require a depressed/uplifted (with respect to PREM) 660-km discontinuity in order to counterbalance the effect of the relatively high/low velocity. If we assume that one of the two parameters is fixed, increasing/lowering  $V_s^{TZ}$  has the same effect on the dispersion data as an uplifted/depressed 660-km discontinuity. If there were no trade-offs between the two parameters, the conditional pdf would not change with

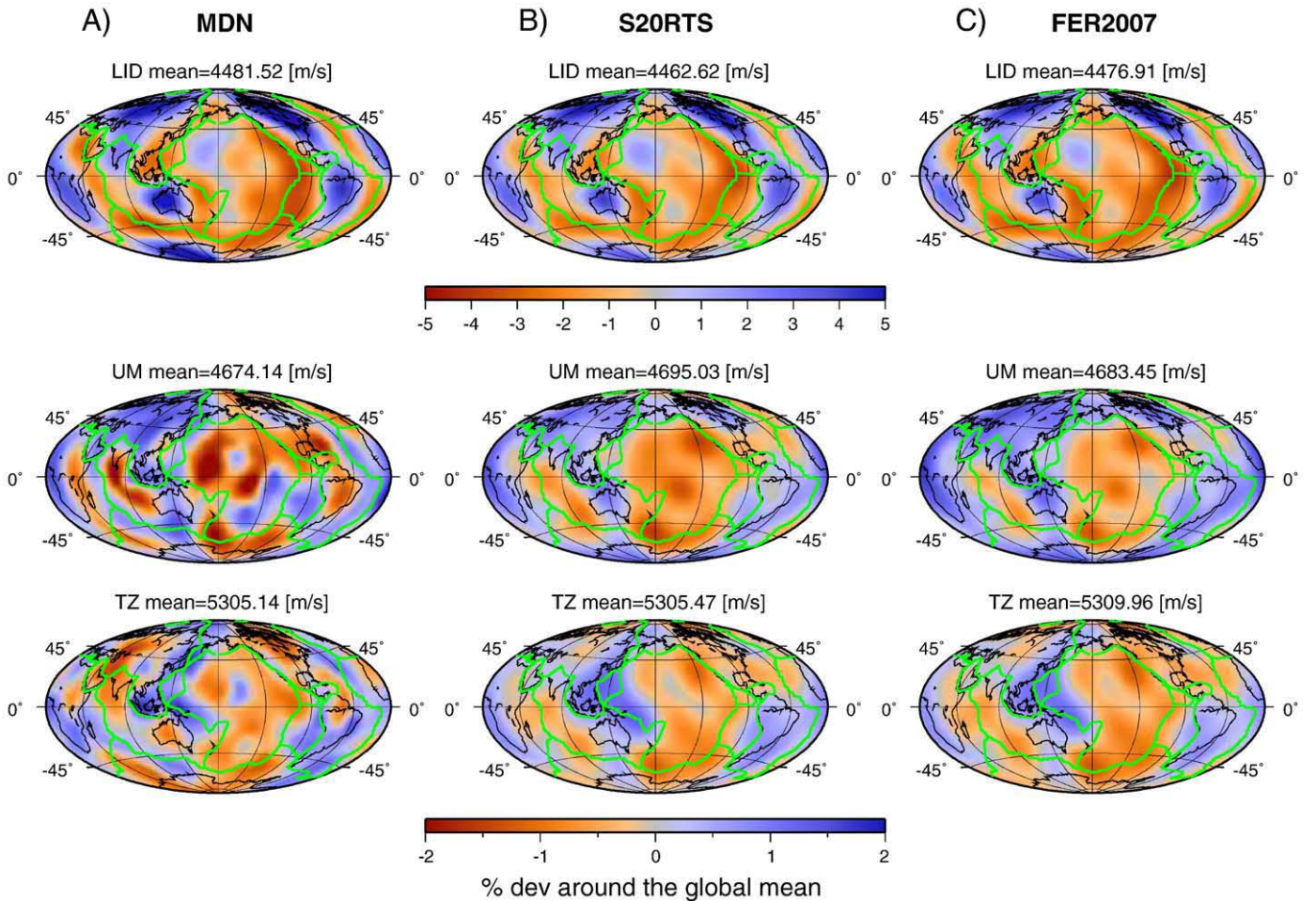


Fig. 4. Comparison of  $V_s^{\text{LID}}$  (top),  $V_s^{\text{UM}}$  (middle) and  $V_s^{\text{TZ}}$  (bottom) between our mean MDN model (A), S20RTS (B) and FER2007 (C). Deviations of the local from the global mean are plotted.

varying  $V_s^{TZ}$ . Furthermore we see that towards relatively low/high  $V_s^{TZ}$  values the 660-km is better constrained than around the reference PREM value. From the marginal pdf  $p(V_s^{TZ}|\mathbf{d}_{\text{prem}})$  (top, right) it follows however that such extreme values of  $V_s^{TZ}$  are not consistent with the given data ( $\mathbf{d}_{\text{prem}}$ ). Note how the maximum of the marginal pdf corresponds well with the true value of the underlying PREM model (dashed). Combining the conditional pdf (top, left) with the marginal pdf (top, right) according to Eq. (2) we then obtain the joint pdf  $p(H_{660}, V_s^{TZ}|\mathbf{d}_{\text{prem}})$  (bottom, right), representing all the information we have about the 660-km topography as well as  $V_s^{TZ}$ . Integrating the joint pdf over  $V_s^{TZ}$  we obtain the marginal pdf  $p(H_{660}|V_s^{TZ}, \mathbf{d}_{\text{prem}})$  (bottom, left (red)) that agrees very well with the marginal pdf (blue) as approximated by a separate MDN directly. This exercise not only demonstrates that our algorithm works correctly, but also illustrates how in forming the joint pdf the uncertainties in  $V_s^{TZ}$  and the trade-offs between 660-km topography and  $V_s^{TZ}$  are taken into account. Trade-offs between other parameters are shown in Meier (2008). The existing trade-offs are not removed, but they are incorporated in our marginal pdf and contribute to the posterior uncertainties (i.e. broadness of the marginal 660-km pdf).

## 6. Results

So far we inverted synthetic dispersion curves and the underlying models were known. In this section we invert dispersion curves at 492 geographic locations evaluated, up to spherical harmonic degree 8, from phase velocity maps provided by Visser et al. (2008a). Degree 8 has been chosen because the long wavelength phase velocity maps are relatively independent of any regularization for all overtones. From the resulting 492 posterior pdfs of the parameter of interest, we can construct global models of any desired statistic with a lateral resolution equivalent to a spherical harmonic expansion of degree 8 (> 5000 km).

### 6.1. S-wave velocity models

Since our approach is radically different from classical seismic tomography, we compared our depth-averaged global velocity models with two other global S-wave velocity models: S2ORTS (Ritsema et al., 1999) and FER2007 (Ferreira et al., 2007). These models are evaluated up to spherical harmonic degree 8 at various depths in order to compute the required depth averages  $V_s^{LID}$ ,  $V_s^{UM}$  and  $V_s^{TZ}$ , respectively. In Fig. 4 our mean MDN models (A) are shown together with S2ORTS (B) and FER2007 (C). The overall agreement between all three models is good. Within the LID (top), which is known to be very well constrained by fundamental mode surface waves (e.g. Ritsema et al., 2004), the four models seem to be literally identical with correlation coefficients  $R > 0.9$  (see Table 1). With increasing depth the large scale

**Table 1**  
Correlation coefficients of  $V_s^{LID}$ ,  $V_s^{UM}$  and  $V_s^{TZ}$  between our mean MDN model, S2ORTS, and FER2007.

	MDN	S2ORTS	FER2007
$V_s^{LID}$			
MDN	1	0.96	0.98
S2ORTS		1	0.99
FER2007			1
$V_s^{UM}$			
MDN	1	0.64	0.72
S2ORTS		1	0.91
FER2007			1
$V_s^{TZ}$			
MDN	1	0.53	0.60
S2ORTS		1	0.83
FER2007			1

**Table 2**  
Percentage of the  $V_s^{LID}$ ,  $V_s^{UM}$  and  $V_s^{TZ}$  estimates from S2ORTS, and FER2007 at the 492 locations that are within  $\pm 1\sigma$  of our MDN model.

	S2ORTS	FER2007
$V_s^{LID}$	57.5%	82.5%
$V_s^{UM}$	64.0%	76.8% <sup>^</sup>
$V_s^{TZ}$	75.6%	76.6%

features of the three models agree still quite well. There are fast velocity anomalies under continents and slow velocity anomalies under oceans in the upper mantle (middle). Furthermore the fast velocity anomalies at subduction zones within the transition zone (bottom) are visible in all three models. There are however some differences, most notably beneath the south-eastern Pacific in the upper mantle (middle), where our MDN model shows slow velocity anomalies which are not visible in any of the other two models. In Table 1 the correlation coefficients between the three models at the various depth ranges are summarized. The correlations between the models generally decrease with increasing depth. It is worth noting that our MDN model correlates best over all three depth ranges with FER2007, who inverted a similar data set. Correlations between the S2ORTS and FER2007 are better than with our MDN model. This might be due to the fact that we performed a nonlinear inversion for absolute values whereas the other two models are obtained from a linearized inversion for model perturbations with respect to a reference model. Additionally the resolving power of seismic data generally decreases with depth and as a consequence the resulting models depend increasingly on prior information (regularization).

Having full pdfs we can also check how many of the 492 S-wave velocity estimates from S2ORTS and FER2007 are within  $\pm 1\sigma$  of our MDN model. The outcome of this analysis is summarized in Table 2, where the percentages of the respective models that are within  $\pm 1\sigma$  of our MDN model are listed over all three depth ranges. Percentage of overlap as well as the correlation coefficients have been computed from absolute model values rather than deviations from a mean. If two models are statistically identical we would expect 66% of the 492 samples to be within  $\pm 1\sigma$ . Whereas the correlation coefficients were generally decreasing with increasing depth (Table 1), this measure tells us that our MDN models are statistically equivalent to FER2007 over all three depth ranges, and that agreement between our MDN model and S2ORTS is best in the transition zone and worst in the LID. The implication of this analysis is, that correlation coefficients are bad indicators of similarity since they only consider single model values (e.g., the mean model) rather than the complete pdf or uncertainty distribution.

### 6.2. Transition zone discontinuities

Encouraged by our S-wave models we trained a MDN on the 660-km topography, inverted dispersion curves at 492 geographic locations and computed mean, standard deviation and information gain from the resulting posterior 660-km topography pdfs (Fig. 5A). The global mean depth of the 660-km discontinuity is 659 km and agrees well with average 660-km discontinuity depth estimates from other studies (e.g. Shearer, 2000). The higher the information gain the more the posterior pdfs differ from the prior pdf and the better the 660-km topography is resolved (Meier et al., 2007a). Generally a higher information gain corresponds to a relatively smaller standard deviation. Interestingly regions of 660-km topography that uplift, as observed over large parts of the Pacific Ocean and along the plate boundaries, seem to be better resolved than regions of a depressed 660-km topography, as observed at the subduction zones in the western Pacific, in South- and North America and in Africa. The large scale features, such as the uplift of the 660-km topography in the Pacific Ocean as well as the depression of the 660-km topography in the western Pacific, South- and North America, agree well with

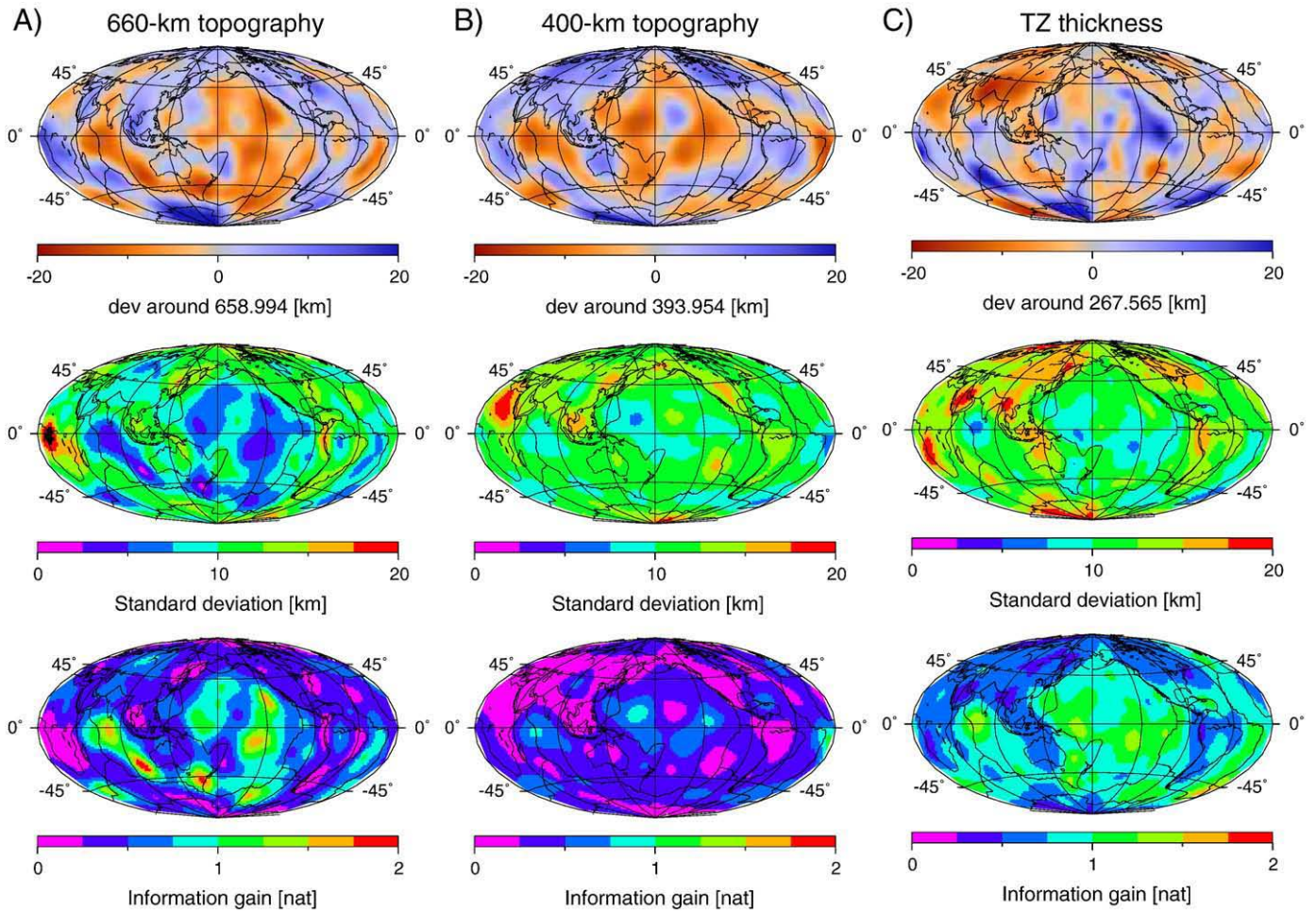


**Fig. 5.** Global models of the 660- (A), 400-km discontinuity (B) and transition zone thickness (C). Mean topography deviation from the global mean (top) together with the standard deviations (middle) and the information gain of the posterior pdfs with respect to the prior pdf (bottom).

TOPOTZ (Flanagan and Shearer, 1998a) and S362ANI (Kustowski et al., 2008) (Fig. 6). The two latter models are constrained by SS-precursors whereas our model is solely constrained by surface wave overtones. The main differences are beneath Africa, where our model shows a depressed 660-km topography, S362ANI shows a slight depression, and TOPOTZ an uplift. The agreement of the large scale features of the 660-km topography, especially between our mean MDN model and S362ANI, suggests that SS precursor measurements are consistent with surface wave overtone measurements. Because SS-precursors and surface waves sense the discontinuity differently, the agreement suggests that the 660-km discontinuity is indeed narrow. From the 660-km estimates of TOPOTZ and S362ANI at the 492 locations, 55.7% and 50.8% are within  $\pm 1\sigma$  of our MDN model respectively. The mean 660-km topography (Fig. 5A) seems to be positively correlated with  $V_s^{TZ}$  (Fig. 4A, bottom), the correlation coefficients are however too low to justify an in-depth discussion on possible causes (i.e.  $R=0.2722$  and  $R=0.4222$  for models expanded up to spherical harmonic degrees 8 and 2, respectively).

Globally we find a positive correlation between our 660- and 400-km topography (Fig. 5B), indicating that not only thermal effects influence the discontinuity topography. In specific areas, such as near the subduction zones in eastern Asia and underneath South America we observe a depression in both the 660-, and the 400-km topography. Over large parts of the Pacific ocean on the other hand we observe an uplift in both the 660- and the 400-km topography. A similar observation was made beneath South America, where a depression in both the 400- and 660-km topography has been reported and explained with possible

chemical heterogeneities influencing the 400-km topography (Schmerr and Garnero, 2007). Agreement between our mean 400-km MDN model and three other global models, TOPOTZ (Flanagan and Shearer, 1998a), S362ANI (Kustowski et al., 2008) and OXFORD (Chambers et al., 2005) is remarkably poor (Table S2 and Fig. 7). Indeed, from the 400-km estimates of TOPOTZ, S362ANI and OXFORD at the 492 locations, only 30.1%, 7.9% and 37.8% are within  $\pm 1\sigma$  of our MDN model respectively. Although TOPOTZ, S362ANI and OXFORD are all based on SS-precursors, agreement between them is just as poor. The most striking difference between our MDN model and the other three is the globally averaged discontinuity depth. We find an average 400-km depth of  $394 \pm 7$  km in comparison to 418 km in TOPOTZ, 410 km (fixed) in S362ANI and 409 km in OXFORD. We suggest that the most likely explanation for this discrepancy is that underside reflections see the bottom part and surface waves the top part of a broad 400-km discontinuity. If the discontinuity occurs over a certain depth, i.e. a gradient, depending on frequency, waves arriving from the bottom will sense a significant impedance contrast differently to waves arriving from the top (surface waves can be seen as constructively interfering reflections from the top). A narrow discontinuity should be seen in a similar way by up- or down-going waves. The details of the necessary gradient and frequency content will need to be established in a theoretical study. A first guess of such a width is to define the average broadness of the 400-km discontinuity as the difference between our mean MDN depth of  $394 \pm 7$  km and the mean depth of 418 km from TOPOTZ to give an average broadness of 17–31 km.

Finally we compare the power spectra for the various 660-, and 400-km topography models considered in this study. We evaluated all

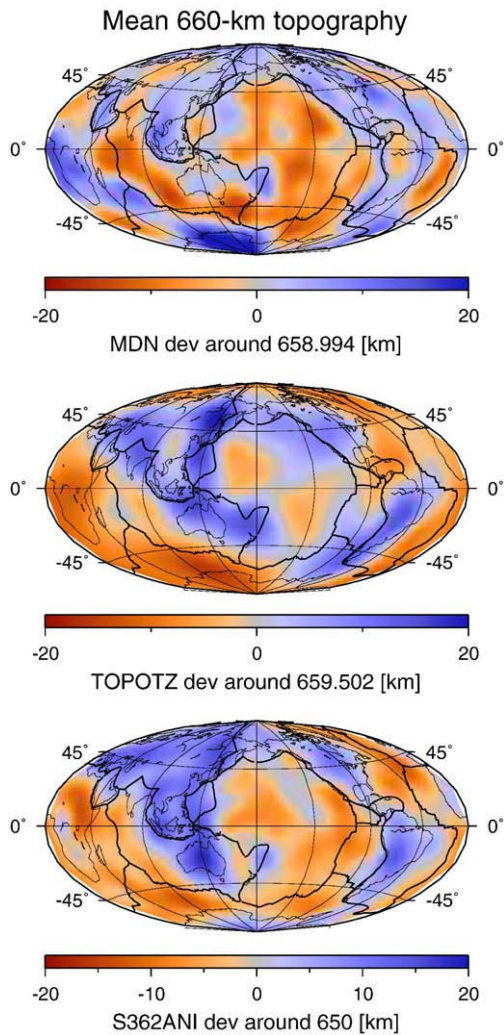


Fig. 6. Three different global models of the 660-km topography: (top) Our mean MDN model; (middle) TOPOTZ; (bottom) S362ANI.

models at 492 geographic locations and performed a spherical harmonic expansion up to degree 8. The power spectra of the three 660-km topography models are plotted in Fig. 8A, whereas the power spectra of the four different 400-km topography models are shown in Fig. 8B. It is interesting to note, that compared to S362ANI and TOPOTZ, the power spectra of our MDN models are much flatter. This might be due to a laterally more homogeneous sampling of surface wave data compared to underside reflections. The uneven sampling in underside reflection studies could bias the spectra towards lower degrees.

### 6.3. Temperature and water content variations within the transition zone

Global scale S-wave velocity anomalies together with topographic variations of the 400- and 660-km discontinuities have mostly been interpreted as thermal in origin (Gu et al., 1998; Flanagan and Shearer, 1998a). The phase transitions, however, not only depend on temperature but also on composition and water content (Litasov et al., 2006). Lateral velocity variations in the transition zone may also be caused by variations in hydration rather than variations in temperature (Smyth and Jacobsen, 2006). Other compositional effects are neglected mainly for convenience, but we are well aware that this is a simplifying assumption. However, according to Matsukage et al. (2005) compositional effects on S-wave velocities are small below a depth of 120 km. Regarding compositional effects on the pressure of phase changes and hence on the topography of the transition zone discontinuities, Suetsugu et al. (2006) noted that iron content has a small effect on the phase transformation from ringwoodite to perovskite and magnesiowüstite (660-km discontinuity), but a significant effect on the olivine to wadsleyite phase transformation (400-km discontinuity). Furthermore there are other compositional effects that might influence S-wave velocities as well as transition zone topographies. Xu et al. (2008) showed for example that S-wave velocities of a mantle comprised of an equilibrium assemblage of pyrolytic composition differs significantly from a mantle comprised of a mechanical mixture of basalt and harzburgite. Despite the fact that neglecting chemical variations might introduce some bias in the resulting models, we used transition zone thickness (Fig. 5C, better constrained than the individual discontinuities, see information gain)

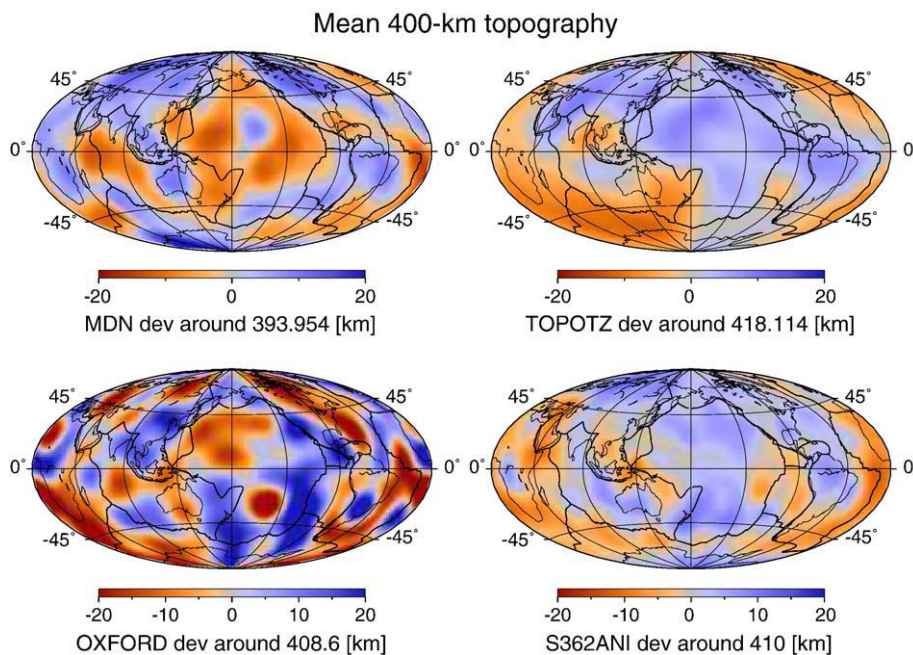


Fig. 7. Four different global models of the 400-km topography. (top, left) Our mean MDN model, (top, right) TOPOTZ, (bottom, left) OXFORD and (bottom, right) S362ANI.

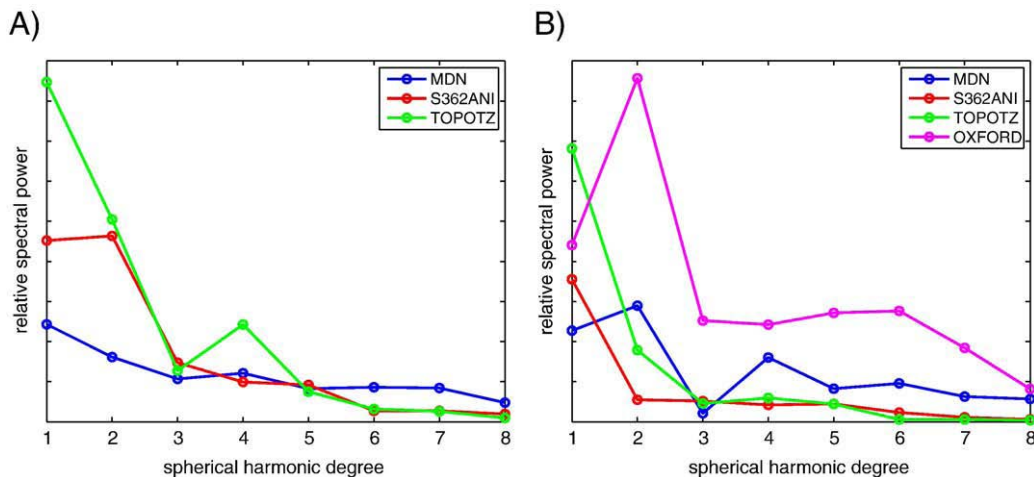


Fig. 8. Relative spectral power as a function of spherical harmonic degree for three different 660-km topography models (left) and four different 400-km topography models (right).

and average S-wave velocity variations (Fig. 4 bottom, left) to estimate variations in temperature and water content. Assuming a linear relationship between seismic parameters and target parameters we may write:

$$\begin{aligned} \delta d &= \frac{\partial d}{\partial T} \delta T + \frac{\partial d}{\partial H_2O} \delta H_2O, \\ \delta \ln V_s &= \frac{\partial \ln V_s}{\partial T} \delta T + \frac{\partial \ln V_s}{\partial H_2O} \delta H_2O, \end{aligned} \quad (3)$$

where  $\delta d$  and  $\delta \ln V_s$  are perturbations in transition zone thickness and S-wave velocity with respect to their global averages from our global MDN models. The partial derivatives are taken from experimental studies:  $\partial d/\partial T = -0.19 \pm 0.05$  km/K (Litasov et al., 2006);  $\partial d/\partial H_2O = 14.5 \pm 7.25$  km/wt.% (Litasov et al., 2006);  $\partial \ln V_s/\partial T = -6 \pm 2 \times 10^{-5} K^{-1}$  (Stixrude and Lithgow-Bertelloni, 2005);  $\partial \ln V_s/\partial H_2O = -0.021 \pm 0.002$  1/wt.% (Smyth and Jacobsen, 2006). Note that these partial derivatives are for an average transition zone thickness and not

just at 410 km or 660 km depth. The unknowns  $\delta T$  and  $\delta H_2O$  are local perturbations with respect to a global unspecified average and correspond to vertical averages over the transition zone. The partial derivatives are assumed to be Gaussian distributed with mean and standard deviation as above. At each of the 492 geographic locations, we generated 10000 independent random samples for each of the four Gaussian partial derivatives and for  $\delta d$  and  $\delta \ln V_s$ , drawn from the corresponding posterior pdfs, and we solved Eq. (3). We thus obtain at each geographic location the posterior pdfs for  $\delta T$  and  $\delta H_2O$  containing the uncertainties in transition zone thickness and S-wave velocity as well as in the experimentally determined partial derivatives. The corresponding means and standard deviations of the temperature and water content variations in the transition zone are shown in Fig. 9. Note that temperature and water content variations correspond to vertical averages over the transition zone with a lateral resolution of spherical harmonic degree 8 (> 5000 km). The subduction zones in the Western Pacific and South America correspond, as expected, to relatively cold temperatures. Beneath continental regions such as Africa, Eurasia and North America as well as over large parts of the Pacific relatively warmer

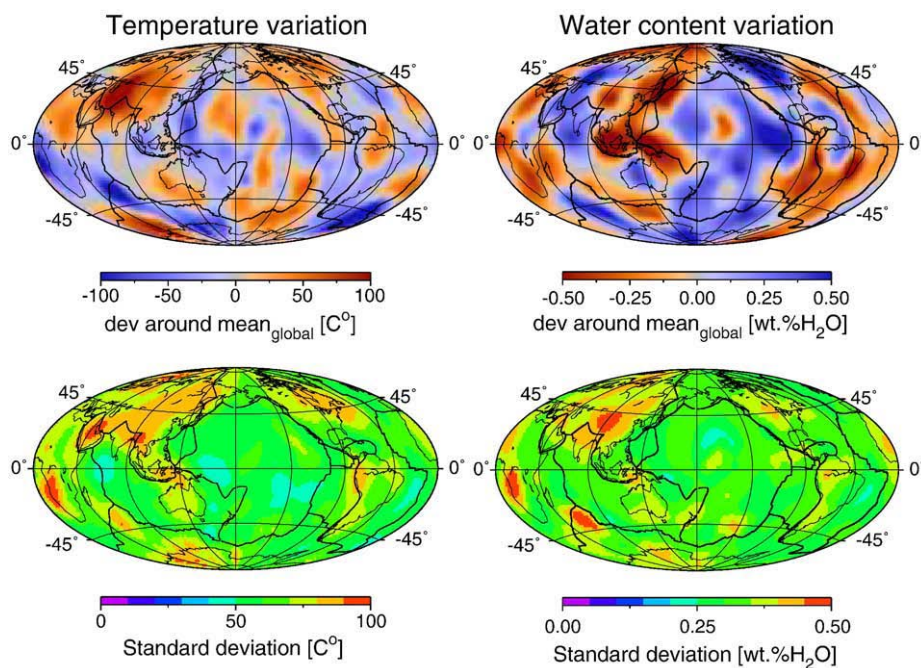


Fig. 9. Mean temperature (left) and water content (right) deviation from the unknown global mean within the transition zone (top) together with the standard deviations (bottom).

temperatures are observed. The temperature variations are in the order of  $\pm 100\text{ K}^\circ$  and agree reasonably well with the model from Cammarano and Romanowicz (2007). Water content is relatively low in the subduction zones in the western Pacific and South America and relatively high over large parts of the Pacific ocean and varies between  $\pm 0.5\text{ wt.}\%$ . Although it is generally assumed that water is transported down to the transition zone along slabs, we find that the transition zone is wettest away from subduction zones.

## 7. Conclusion

Our consistent nonlinear inversion of surface wave overtones produced models of shear wave variations and topography of the discontinuities where the natural trade-offs in the problem are accounted for in the uncertainties. Shear wave models and the 660-km topography are statistically indistinguishable from previous models. Our 400-km topography model however is different suggesting a broad discontinuity with an average broadness of 17–31 km. This implies a significant average water content, and a discontinuity consisting of a zone where olivine, wadsleyite and melt co-exist (Hirschmann et al., 2006). This would explain several seismological observations such as the frequency dependence of receiver functions (van der Meijde et al., 2003), some observed double peaks in underside reflections (Deuss and Woodhouse, 2001; Deuss and Woodhouse, 2002; Schmerr and Garnero, 2007) and is possibly related to the recently observed low-velocity layer above the 400-km discontinuity (Song et al., 2004; Jasbinsek and Dueker, 2007; Vinnik and Farra, 2007).

Compared to similar studies that estimated lateral variations in temperature and water content from tomographic models (e.g. Shito et al., 2006; Suetsugu et al., 2006) the advantage of our approach is that the transition zone thickness and S-wave velocity models are obtained from a joint inversion of the same data set. The resulting maps offer a first step towards a quantitative interpretation of tomographic models in terms of temperature and water content on a global scale. Interpreting these models, one has however to keep in mind that they are vertically averaged over the transition zone with a lateral resolution of spherical harmonic degree 8 ( $>5000\text{ km}$ ). The global model of lateral temperature variations (Fig. 9, left) shows, as expected, relatively cold subduction zones and relatively warm continental regions and hot spots. Our model of lateral water content variations (Fig. 9, right) suggests however that the transition zone is wettest away from subduction zones. If water is transported down into the transition zone by slabs and remains close to the narrow slabs, it might not be resolved by our model. The fact that cold subduction zones are seen but wet subduction zones are not, might be an indication that temperature diffuses away from slabs more quickly than water, or that water is not transported down slabs into the transition zone.

## Acknowledgments

We thank Jeroen Ritsema and an anonymous reviewer for comments that helped to improve the manuscript, K. Visser for providing the phase velocity maps and H. Paulssen for many helpful discussions. Some of the figures were generated with Generic Mapping Tools (Wessel and Smith, 1998). The spherical harmonic analyses were performed using the freely available software archive SHTOOLS (available at <http://www.ipgp.jussieu.fr/~wiczor/SHTOOLS/SHTOOLS.html>). U. Meier is grateful for the support of the HPC-Europa programme, funded under the European Commission's Research Infrastructures activity of the Structuring the European Research Area programme, contract number RI3-CT-2003-506079. Computational resources for this work were provided by the Dutch National Science Foundation under grant number NWO: VICI865.03.007 and the Netherlands Research Center for Integrated Solid Earth Science (ISES 3.2.5 High End Scientific Computation Resources).

## Appendix A. Supplementary data

Supplementary data associated with this article can be found, in the online version, at doi:10.1016/j.epsl.2009.03.004.

## References

- Bercovici, D., Karato, S., 2003. Whole-mantle convection and the transition-zone water filter. *Nature* 425, 39–44.
- Bishop, C.M., 1995. *Neural Networks for Pattern Recognition*. Oxford University Press, Oxford, UK.
- Cammarano, F., Romanowicz, B., 2007. Insights into the nature of the transition zone from physically constrained inversion of long-period seismic data. *Proc. Natl. Acad. Sci. U. S. A.* 104, 9139–9144.
- Chambers, K., Woodhouse, J.H., Deuss, A., 2005. Topography of the 410-km discontinuity from PP and SS precursors. *Earth Planet. Sci. Lett.* 235, 610–622.
- Chevrot, S., Vinnik, L., Montagner, J.-P., 1999. Global-scale analysis of the mantle Pds phases. *J. Geophys. Res.* 104 (B9), 20203–20219.
- Collier, J.D., Helffrich, G.R., 1997. Topography of the “410” and “660” km seismic discontinuities in the Izu-Bonin subduction zone. *Geophys. Res. Lett.* 24 (12), 1535–1538.
- Deuss, A., Woodhouse, J., 2001. Seismic observations of splitting of the mid-transition zone discontinuity in Earth's mantle. *Science* 294, 354–357.
- Deuss, A., Woodhouse, J.H., 2002. A systematic search for mantle discontinuities using SS-precursors. *Geophys. Res. Lett.* 29 (8), 1249. doi:10.1029/2002GL014768.
- Devilee, R., Curtis, A., Roy-Chowdhury, K., 1999. An efficient, probabilistic neural network approach to solving inverse problems: inverting surface wave velocities for Eurasian crustal thickness. *J. Geophys. Res.* 104 (B12), 28841–28857. December.
- Dziewonski, A.M., Anderson, D.L., 1981. Preliminary reference Earth model. *Phys. Earth Planet. Inter.* 25, 297–356.
- Ferreira, A.M., Woodhouse, J.H., Visser, K., Trampert, J., 2007. Investigating the anisotropic shear wave velocity structure of the Earth's mantle. *EOS Trans. AGU* 88 (52).
- Flanagan, M.P., Shearer, P.M., 1998a. Global mapping of topography on transition zone velocity discontinuities by stacking SS precursors. *J. Geophys. Res.* 103 (B2), 2673–2692.
- Flanagan, M.P., Shearer, P.M., 1998b. Topography on the 410-km seismic velocity discontinuity near subduction zones from stacking of sS, sP and pP precursors. *J. Geophys. Res.* 103 (B9), 21165–21182.
- Flanagan, M.P., Shearer, P.M., 1999. A map of topography on the 410-km discontinuity form PP precursors. *Geophys. Res. Lett.* 26 (5), 549–552.
- Frost, D.J., Dolejš, D., 2007. Experimental determination of the effect of H<sub>2</sub>O on the 410-km seismic discontinuity. *Earth Planet. Sci. Lett.* 256, 182–195.
- Gossler, J., Kind, R., 1996. Seismic evidence for very deep roots of continents. *Earth Planet. Sci. Lett.* 138, 1–13.
- Gu, Y., Dziewonski, A.M., 2002. Global variability of transition zone thickness. *J. Geophys. Res.* 107 (B7). doi:10.1029/2001JB000489.
- Gu, Y., Dziewonski, A.M., Agee, C.B., 1998. Global de-correlation of the topography of transition zone discontinuities. *Earth Planet. Sci. Lett.* 157, 57–67.
- Gu, Y., Dziewonski, A.M., Ekström, G., 2003. Simultaneous inversion for mantle shear velocity and topography of transition zone discontinuities. *Geophys. J. Int.* 154, 559–583.
- Helffrich, G., 2000. Topography of the transition zone seismic discontinuities. *Rev. Geophys.* 38, 141–158.
- Hirschmann, M.M., Withers, A.C., Aubaud, C., 2006. Petrologic structure of a hydrous 410 km discontinuity. *Geophys. Monogr.* 168, 277–287.
- Jasbinsek, J., Dueker, K., 2007. Ubiquitous low-velocity layer atop the 410-km discontinuity in the northern Rocky Mountains. *Geochem. Geophys. Geosyst.* 8 (Q10004). doi:10.1029/2007GC001661.
- Kustowski, B., Ekström, G., Dziewonski, A.M., 2008. Anisotropic shear-wave velocity structure of the Earth's mantle: a global model. *J. Geophys. Res.* 113 (B06306). doi:10.1029/2007JB005169.
- Lawrence, J.F., Shearer, P.M., 2006. A global study of transition zone thickness using receiver functions. *J. Geophys. Res.* 111 (B06307). doi:10.1029/2005JB003973.
- Lebedev, S., Chevrot, S., van der Hilst, R.D., 2002. Seismic evidence for olivine phase changes at the 410- and 660-kilometer discontinuities. *Science* 296, 1300–1302.
- Lebedev, S., Chevrot, S., van der Hilst, R.D., 2003. Correlation between the shear-speed structure and thickness of the mantle transition zone. *Phys. Earth Planet. Int.* 136, 25–40.
- Litasov, K.D., Ohtani, E., Sano, A., 2006. Influence of water on major phase transitions in the Earth's mantle. *Geophys. Monogr.* 168, 95–111.
- Matsukage, K.N., Nishihara, Y., Karato, S., 2005. Seismological signature of chemical differentiation of Earth's upper mantle. *J. Geophys. Res.* 110, B12305.
- Meier, U., 2008. Bayesian inversion of surface wave data for discontinuities and velocity structure in the upper mantle using Neural Networks. Ph.D. thesis, Utrecht University.
- Meier, U., Curtis, A., Trampert, J., 2007a. Fully nonlinear inversion of fundamental mode surface waves for a global crustal model. *Geophys. Res. Lett.* 34, L16304. doi:10.1029/2007/GL030989.
- Meier, U., Curtis, A., Trampert, J., 2007b. Global crustal thickness from neural network inversion of surface wave data. *Geophys. J. Int.* 169, 706–722.
- Panning, M., Romanowicz, B., 2006. A three-dimensional radially anisotropic model of shear velocity in the whole mantle. *Geophys. J. Int.* 167, 361–379.
- Petersen, N., Gossler, J., Kind, R., Stammer, K., Vinnik, L., 1993. Precursors to SS and structure of transition zone of the north-western Pacific. *Geophys. Res. Lett.* 20 (4), 281–284.
- Ritsema, J., van Heijst, H.J., Woodhouse, J.H., 1999. Complex shear wave velocity structure imaged beneath Africa and Iceland. *Science* 286 (5446), 1925–1928.

- Ritsema, J., van Heijst, H.J., Woodhouse, J.H., 2004. Global transition zone tomography. *J. Geophys. Res.* 109 (B02302). doi:10.1029/2003JB002610.
- Ritsema, J., Xu, W., Stixrude, L., Lithgow-Bertelloni, C., 2008. Estimates of the transition zone temperature in a mechanically mixed upper mantle. *Earth Planet. Sci. Lett.* doi:10.1016/j.epsl.2008.10.024.
- Schmerr, N., Garnero, E., 2006. Investigation of upper mantle discontinuity structure beneath the central Pacific using SS precursors. *J. Geophys. Res.* 111, B088305. doi:10.1029/2005JB004197.
- Schmerr, N., Garnero, E., 2007. Upper mantle discontinuity topography from thermal and chemical heterogeneity. *Science* 318, 623–626.
- Shearer, P.M., 2000. Upper mantle seismic discontinuities. *Geophys. Monogr.* 117, 115–131.
- Shearer, P.M., Masters, T.G., 1992. Global mapping of topography on the 660-km discontinuity. *Nature* 355, 791–796.
- Shito, A., Karato, S., Matsukage, K.N., Nishihara, Y., 2006. Towards mapping the three-dimensional distribution of water in the upper mantle from velocity and attenuation tomography. *Geophys. Monogr.* 168, 225–236.
- Smyth, J.R., Jacobsen, S.D., 2006. Nominally anhydrous minerals and Earth's deep water cycle. *Geophys. Monogr.* 168, 1–11.
- Song, T.-R. A., Helmberger, D.V., Grand, S.P., 2004. Low-velocity zone atop the 410-km seismic discontinuity in the northwestern United States. *Nature* 427, 530–533.
- Stixrude, L., Lithgow-Bertelloni, C., 2005. Thermodynamics of mantle minerals — I. Physical properties. *Geophys. J. Int.* 162. doi:10.1111/j.1365-246X.2005.02642.x.
- Suetsugu, D., Inoue, T., Yamada, A., Zhao, D., Obayashi, M., 2006. Towards mapping the three-dimensional distribution of water in the transition zone from P-velocity tomography and 660-km discontinuity depths. *Geophys. Monogr.* 168, 237–249.
- Tauzin, B., Debayle, E., Wittlinger, G., 2008. The mantle transition zone as seen by global Pds phases: no clear evidence for a thin transition zone beneath hotspots. *J. Geophys. Res.* 113 (B08309). doi:10.1029/2007JB005364.
- Trampert, J., Spetzler, J., 2006. Surface wave tomography: finite-frequency effects lost in the null space. *Geophys. J. Int.* 164, 394–400.
- van der Meijde, M., Marone, F., Giardini, D., van der Lee, S., 2003. Seismic evidence for water deep in Earth's upper mantle. *Science* 300, 1556–1558.
- Vidale, J.E., Benz, H.M., 1992. Upper-mantle seismic discontinuities and the thermal structure of subduction zones. *Nature* 356, 678–682.
- Vinnik, L., Farra, V., 2007. Low S velocity atop the 410-km discontinuity and mantle plumes. *Earth Planet. Sci. Lett.* 262, 398–412.
- Visser, K., Trampert, J., Kennett, B.L.N., 2008a. Global anisotropic phase velocity maps for higher mode Love and Rayleigh waves. *Geophys. J. Int.* 172. doi:10.1111/j.1365-246X.2007.03714.x.
- Visser, K., Trampert, J., Lebedev, S., Kennett, B.L.N., 2008b. Probability of radial anisotropy in the deep mantle. *Earth Planet. Sci. Lett.* 270, 241–250.
- Wang, Z., Dahlen, F.A., 1995. Spherical-spline parameterization of three-dimensional Earth models. *Geophys. Res. Lett.* 22 (22), 3099–3102.
- Wessel, P., Smith, W.H.F., 1998. New, improved version of Generic Mapping tools released. *EOS Trans. AGU* 79 (47), 579.
- Woodhouse, J.H., 1974. Surface waves in laterally varying layered structure. *Geophys. J. R. Astron. Soc.* 37, 461–490.
- Woodhouse, J.H., 1988. The calculation of eigenfrequencies and eigenfunctions of the free oscillations of the Earth and the Sun. *Seismological Algorithms, Computational Methods and Computer Programs*. Academic Press, London, UK, pp. 321–370.
- Xu, W., Lithgow-Bertelloni, C., Stixrude, L., Ritsema, J., 2008. The effect of bulk composition and temperature on mantle seismic structure. *Earth Planet. Sci. Lett.* 275, 70–79.